

The toroidicity-induced Alfvén eigenmode structure in DIII-D: Implications of soft x-ray and beam-ion loss data

E. M. Carolipio, W. W. Heidbrink, C. Z. Cheng, M. S. Chu, G. Y. Fu, A. Jaun, D. A. Spong, A. D. Turnbull, and R. B. White

Citation: [Physics of Plasmas](#) **8**, 3391 (2001); doi: 10.1063/1.1378066

View online: <https://doi.org/10.1063/1.1378066>

View Table of Contents: <http://aip.scitation.org/toc/php/8/7>

Published by the [American Institute of Physics](#)

Articles you may be interested in

[Properties of toroidal Alfvén eigenmode in DIII-D plasma](#)

[Physics of Plasmas](#) **22**, 022509 (2015); 10.1063/1.4908274

[Measurements and modeling of Alfvén eigenmode induced fast ion transport and loss in DIII-D and ASDEX Upgrade](#)

[Physics of Plasmas](#) **18**, 056114 (2011); 10.1063/1.3574663

[Basic physics of Alfvén instabilities driven by energetic particles in toroidally confined plasmas](#)

[Physics of Plasmas](#) **15**, 055501 (2008); 10.1063/1.2838239

[What is the “beta-induced Alfvén eigenmode?”](#)

[Physics of Plasmas](#) **6**, 1147 (1999); 10.1063/1.873359

[Fast-ion transport by Alfvén eigenmodes above a critical gradient threshold](#)

[Physics of Plasmas](#) **24**, 056109 (2017); 10.1063/1.4977535

[Global Alfvén modes: Theory and experiment*](#)

[Physics of Fluids B: Plasma Physics](#) **5**, 2546 (1993); 10.1063/1.860742

PHYSICS TODAY

WHITEPAPERS

MANAGER'S GUIDE

Accelerate R&D with
Multiphysics Simulation

READ NOW

PRESENTED BY

 **COMSOL**

The toroidicity-induced Alfvén eigenmode structure in DIII-D: Implications of soft x-ray and beam-ion loss data

E. M. Carolipio and W. W. Heidbrink^{a)}

Department of Physics and Astronomy, University of California, Irvine, California 92697

C. Z. Cheng

Princeton Plasma Physics Laboratory, Princeton University, P.O. Box 451, Princeton, New Jersey 08544

M. S. Chu

General Atomics, P.O. Box 85608, San Diego, California 92186-9784

G. Y. Fu

Princeton Plasma Physics Laboratory, Princeton University, P.O. Box 451, Princeton, New Jersey 08544

A. Jaun

Alfvén Laboratory, Royal Institute of Technology, Stockholm, Sweden

D. A. Spong

Oak Ridge National Laboratory, Oak Ridge, Tennessee 37831-8071

A. D. Turnbull

General Atomics, P.O. Box 85608, San Diego, California 92186-9784

R. B. White

Princeton Plasma Physics Laboratory, Princeton University, P.O. Box 451, Princeton, New Jersey 08544

(Received 30 January 2001; accepted 17 April 2001)

The internal structure of the toroidicity-induced Alfvén eigenmode (TAE) is studied by comparing soft x-ray profile and beam ion loss data taken during TAE activity in the DIII-D tokamak [W. W. Heidbrink *et al.*, Nucl. Fusion **37**, 1411 (1997)] with predictions from theories based on ideal magnetohydrodynamic (MHD), gyrofluid, and gyrokinetic models. The soft x-ray measurements indicate a centrally peaked eigenfunction, a feature which is closest to the gyrokinetic model's prediction. The beam ion losses are simulated using a guiding center code. In the simulations, the TAE eigenfunction calculated using the ideal MHD model acts as a perturbation to the equilibrium field. The predicted beam ion losses are an order of magnitude less than the observed $\sim 6\%$ – 8% losses at the peak experimental amplitude of $\delta B_r/B_0 \approx 2\text{--}5 \times 10^{-4}$. © 2001 American Institute of Physics. [DOI: 10.1063/1.1378066]

I. INTRODUCTION

Toroidicity-induced Alfvén eigenmodes (TAEs) are fast-ion driven instabilities that can cause energetic particle losses in tokamaks. These losses are a concern for future devices with reactor-like plasmas since losses significantly degrade performance and escaping particles may cause damage to the vacuum vessel and to plasma-facing components.¹

Theoretical work on the TAE is extensive. Initial papers noted the existence of a spectral gap in the ideal magnetohydrodynamic (MHD) continuum² that supported an eigenmode³ and pointed out that fast ions could destabilize the mode.^{3,4} After the instability was observed experimentally^{5,6} work intensified on understanding the stability properties of the mode. Inclusion of damping effects associated with the coupling to kinetic Alfvén waves^{7–9} gave better agreement with the experimentally observed stability thresholds. These treatments of “continuum” and “radiative” damping employed the global MHD eigenfunction (outside of narrow

damping layers). Subsequent papers stressed modifications of the eigenfunction by kinetic effects. The eigenfunction is altered by coupling to other plasma waves,^{10–12} by energetic particles^{11,13–17} and by sheared rotation profiles.¹⁸

Experimentally, there have been many studies of various properties of the TAE (Ref. 19) but accurate measurements of the TAE eigenfunction are rare. At the Tokamak Fusion Test Reactor (TFTR), beam emission spectroscopy and reflectometry were used to make fluctuation measurements. In the former measurement, the poloidal mode number derived from beam emission spectroscopy was consistent with predictions of ideal MHD to within $\sim 50\%$ uncertainties.²⁰ In the reflectometry measurements, Nazikian *et al.* measured the radial structure of alpha particle driven TAEs over several shots with similar Mirnov activity.²¹ The structure of an $n=4$ TAE had qualitative agreement with a prediction from an ideal MHD model but an $n=2$ TAE which coexisted with the other mode had a core-localized antiballooning structure inconsistent with theory. (n is the toroidal mode number and m is the poloidal mode number.) Reflectometry measurements of an $n=1$ TAE on JT-60U found qualitative agree-

^{a)}Electronic mail: wwheidbr@uci.edu

ment with the expected ballooning structure.²² In DIII-D, a poloidal array of magnetic probes was used to measure fluctuations during TAE activity.²³ Although the amplitude of the fluctuations did not agree with predictions from ideal and resistive MHD models, it compared fairly well with the predictions of a model retaining Landau damping and finite Larmor radius (FLR) effects. For this model, the comparison yielded reduced χ^2 's of 1.2 and 1.6, respectively, for two different toroidal mode numbers. On the W7-AS stellarator, an x-ray imaging system consisting of 200–400 sightlines was used to construct a three-dimensional rendering of the TAE,²⁴ yielding the most detailed picture of the internal TAE mode structure to date. So far, the data have not been compared with theory.

An alternative method of testing theoretically predicted eigenfunctions is to use particle simulations. By following fast ion trajectories in the presence of a perturbation to the equilibrium field, particle transport with different TAE eigenfunctions can be calculated and those losses compared with observations. A study of this type was done in the Poloidal Divertor Experiment for fishbones, an MHD mode with a simpler structure. The model eigenfunction in that case successfully predicted anomalous ^3He losses over a range of mode amplitudes.²⁵ Similar comparisons have been performed for the sawtooth instability^{26,27} and for tearing modes.^{28,29} For the TAE, particle simulation studies have focused on the mode's interaction with alpha particles. Particle simulations have been used to investigate the effect of TAE modes on alpha particle transport in the International Tokamak Engineering Reactor (ITER),³⁰ the nonlinear saturation of the instability due to alpha particle redistribution,³¹ the expected alpha particle diffusion from observed TAEs in the Joint European Torus (JET),³² and the effect of the TAE on fast particles in spherical tokamaks.¹⁷ Unfortunately, in deuterium–tritium (D–T) experiments, no anomalous alpha particle losses were observed in TFTR (Ref. 33) and no alpha-driven TAEs were detected in JET (Ref. 34) D–T experiments, so comparisons between particle simulations and experiment were impossible.

Verification of the theoretical models for the TAE with experimental evidence is necessary in order to have confidence in our ability to use these models to predict high-frequency Alfvén activity in future devices. The investigation reported in this paper is part of the effort to understand the details of the TAE mode structure. In this study, we take two sets of data acquired during a DIII-D discharge with TAE activity (shot 71524) and compare them with predictions based on several theoretical models.

The first set of data consists of soft x-ray measurements from two arrays (one array has a vertical view of the plasma while the other has a horizontal view) on DIII-D during TAE activity. These data depend directly on the mode's spatial structure. We compare them with the expected soft x-ray emission from the $n=5$ linear eigenfunctions generated by codes based on ideal MHD, gyrofluid and gyrokinetic models. The models and the discharge are described in detail in Sec. II while specifics of the comparison and the results are given in Sec. III. The data show an eigenfunction with a strongly peaked amplitude in the center, similar to the struc-

ture implied by measurements from a poloidal array of Mirnov coils.²³ The gyrokinetic prediction compares well with the data qualitatively but quantitative discrepancies exist, although these may be accounted for by uncertainties in the modeling.

The second set of data is the 2.5 MeV neutron signal during TAE bursts. Drops in this signal imply significant losses of beam ions. To properly make this comparison, we use a guiding center code to simulate fast ion motion in the presence of TAE activity, similar to the work done for fishbones on PDX.²⁵ Here, the TAE eigenfunction is generated using the ideal MHD model and introduced in the code as a time dependent perturbation to the equilibrium. Particle losses over a range of amplitudes are calculated and compared with losses in the range of experimental mode amplitudes (Sec. IV). The particle simulations predict only a fraction of the losses measured in the experiment.

A discussion on possible reasons why the data do not compare well with theoretical predictions, and the consequences, is presented in Sec. V. Conclusions from this study are summarized in Sec. VI.

II. THEORETICAL MODELING

For this study we select a well-documented DIII-D discharge, shot 71524. This discharge is a low field (0.8 T), inner-wall limited deuterium plasma of moderate elongation (1.6) that is heated by 5 MW of deuterium neutral beams. The flux surfaces and kinetic profiles appear in Figs. 3–5 of Ref. 35 and the time evolution in Refs. 36 and 37. The TAE activity occurs in ~ 1 ms bursts separated by ~ 8 ms; the cycle resembles those shown in Ref. 38 and is caused by beam-ion losses. (The escaping particles are observed to reach the vessel wall.) Each burst contains a “cluster” of several toroidal modes with mode numbers n ranging from 1 to 9.³⁵ The Fourier spectrum and the Alfvén gap structure³⁹ for one of the bursts are shown in Fig. 1. The splitting of the peaks in the spectrum is caused by the Doppler shift although for some of the bursts each peak in the spectrum contains more than one toroidal mode.³⁶ If one assumes that different toroidal modes are excited in the same region in the plasma, the spectral data indicate that the mode is excited near the $q=1$ surface [Fig. 1(b)]. The inferred frequency in the plasma frame is near the bottom of the toroidicity-induced gap and may actually lie in the continuum. The dominant toroidal mode numbers in the TAE feature are usually $n=3-5$. Although fishbone activity is also present [Fig. 1(a)], the TAEs are primarily responsible for beam-ion transport.⁴⁰ The drop in the neutron emission at the burst analyzed in Sec. IV indicates that an $\sim 8\%$ loss of the injected beam particles occurs.

Three separate wave codes that feature different physical models are used to calculate the linear response of the plasma. (Only one of the codes is used for the particle simulation analysis, see Sec. IV.) None of the models takes into account the effect of the energetic ions on the mode structure. In the calculations, all three codes use a numerical equilibrium that is based on the experimental equilibrium fitting code EFIT.⁴¹

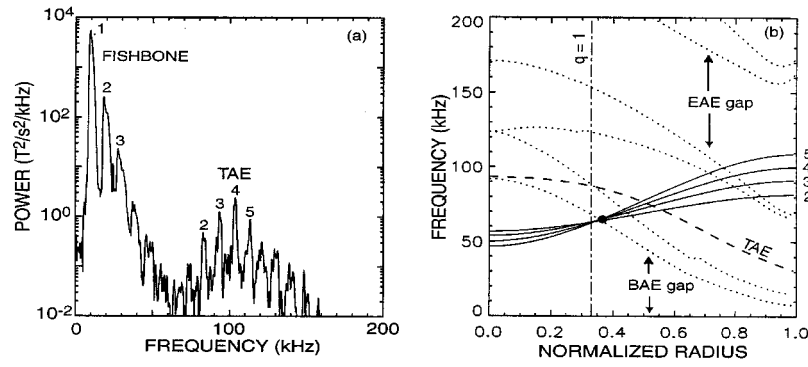


FIG. 1. (a) Cross-power spectrum from a pair of magnetic probes at 1883–1886 ms in discharge 71524. The numbers by the spectral peaks represent the toroidal mode numbers obtained from a toroidal array of eight unequally spaced probes. The low frequency feature with the dominant $n=1$ peak is a fishbone oscillation; the cluster of spectral peaks around 100 kHz is the TAE feature. (b) Radial profiles of Doppler-shift-corrected frequencies $f_{lab} - nf_{rot}$ for the TAE feature. Here f_{lab} is the measured frequency in the laboratory frame and f_{rot} is the measured toroidal rotation frequency. If one assumes that the different toroidal mode numbers have the same frequency in the plasma frame f_{pl} , the intersection of the curves (indicated by the solid dot) is f_{pl} . Also shown are the frequency of the center of the TAE gap $v_A/4\pi qR$ (dashed line), the radial location of the $q=1$ surface (dashed-dotted line), and the envelopes of the Alfvén continuum as calculated by the CONT code (Ref. 39) (dotted lines). The CONT code includes plasma pressure terms that create a beta-induced (BAE) gap and raise the frequencies of the TAE and ellipticity-induced (EAE) gaps.

The NOVA code⁴² solves the linearized ideal MHD equations using cubic B spline finite elements and a Fourier expansion in a general flux coordinate system. The code was updated to include Landau and radiative damping in its stability model (the NOVA-K code) though the updated version still uses the same “ideal MHD” model to solve for the linear eigenfunction. A search for core localized modes for this discharge was conducted using this updated code but none were found, most likely because the core TAE does not exist in plasmas with a large pressure gradient⁴³ and the experimental pressure gradients are a factor of 2 larger than the critical value. We solve for three unstable eigenfunctions with toroidal mode numbers 3, 4, and 5, all with frequencies of 64 kHz in the plasma frame. The poloidal components ranging from $m=1$ through 15 for the $n=3$ TAE calculated

using NOVA are shown in Fig. 2(a). Though not shown, the solutions for the $n=4$ and 5 modes are qualitatively similar to the $n=3$, peaking around $\psi_p/\psi_{p,edge} \approx 0.93$ but with the $m=10$ and $m=13$ poloidal components being strongest for each n , respectively.

The FAR code⁴⁴ is a program that solves initial value problems in full toroidal geometry. A modified version (TAE/FL) of this code⁴⁵ was used to calculate the linear TAE eigenfunction for this burst. This version uses a “gyrofluid” model that retains ion and electron Landau damping and thermal ion FLR effects but ignores the fast Alfvén wave. The background plasma is modeled using the reduced MHD equations with a consistent Landau closure in slab geometry to account for the energetic species moment equations (retaining the shear Alfvén spectrum and continuum damping)

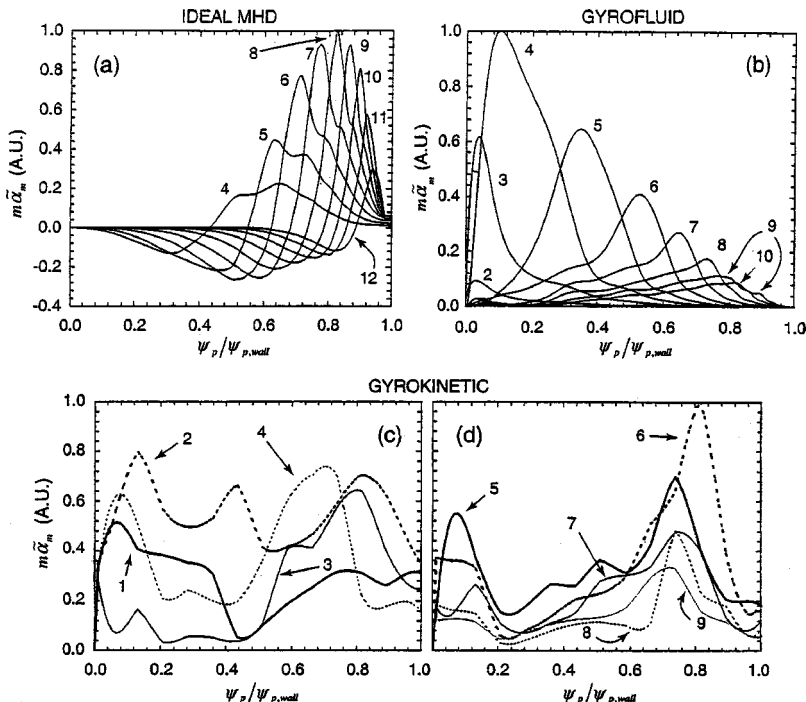


FIG. 2. Comparison of $n=3$ TAE eigenfunctions from three different codes. Plotted are the unnormalized amplitudes of the Fourier decomposed poloidal harmonics as functions of normalized poloidal flux, $\psi_p/\psi_{p,wall}$. The harmonics are given as $m\tilde{\alpha}_m$ since $\delta B_r \sim m\tilde{\alpha}_m/qR$. (a) For the NOVA case, solutions for the $m=1-15$ harmonics are provided (components with amplitudes $<10\%$ of the peak amplitude are not shown) evaluated in a straight-field line coordinate system with a Jacobian $J \sim B^{-2}$. (b) For TAE/FL case, solutions for the $m=1-15$ harmonics are provided (components with amplitudes $<5\%$ of the peak amplitude not shown) in a coordinate system with $J \sim R^{-2}$. Not pictured is the imaginary part of this eigenfunction. (c)–(d) For the PENN case, pictured in (c) are the $m=1-4$ (heavy solid, heavy dashed, light solid, and light dashed trace, respectively) while shown in (d) are the $m=5-9$ harmonics (heavy solid, heavy dashed, light solid, light dashed, and very light solid trace, respectively). This eigenfunction also has radially dependent phases, $\varphi_{nm} = \varphi_{nm}(\psi_p)$, which are not pictured, and was evaluated in the same coordinate system as the NOVA case.

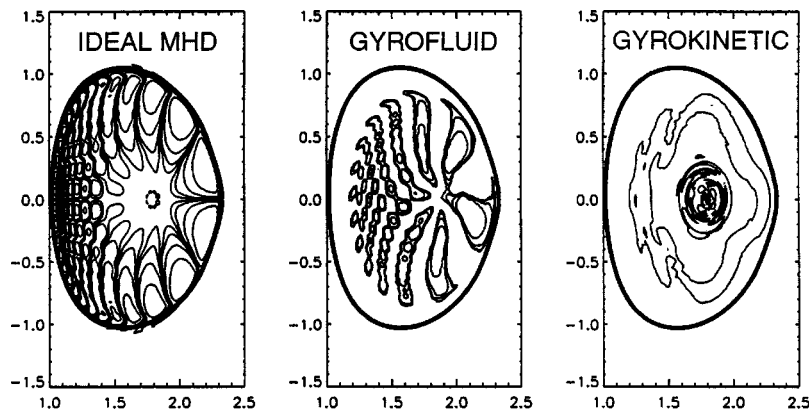


FIG. 3. Logarithmic contours of the amplitude of the $n=5$ eigenfunction calculated by the NOVA, TAE/FL, and PENN codes, respectively. The heavy line is the plasma boundary.

and the assumption that the fast ion distribution is Maxwellian. Linearly unstable modes are found by calculating growth rates of possible modes using an expression derived from the gyrofluid equations. The Fourier components of the real part of the eigenfunction from this code are given in Fig. 2(b).

The PENN code⁴⁶ solves the Maxwell equations using cubic finite elements in the radial and poloidal directions. An oscillating helical source current is distributed inside the plasma to excite bulk modes. (In the experiment, these modes are driven by the energetic beam-ions.) Only eigenmodes with sufficiently small damping and wavefields independent of the excitation are regarded as physically meaningful. The linear response of the plasma is defined in terms of a dielectric tensor featuring a resistive plasma model and a kinetic FLR model that is appropriate for higher temperatures. By taking into account the FLR excursions, the drifts of thermal particles and the resonant Landau interactions, this “gyrokinetic” model not only is well-suited for the propagation of the fast waves but also models the linear mode conversion to the slower waves such as the kinetic Alfvén, the ion acoustic, and drift waves. Several unstable modes with sufficiently small damping were found; the linear response of the plasma in this discharge was calculated for a 62.5 kHz, $n=3$ mode [as shown in Figs. 2(c) and 2(d)] and for a 71 kHz, $n=5$ mode.

The differences in the predicted mode structure (Figs. 2–3) are striking. (Remember, these predictions are for the *same* TAE mode.) Some of these differences are attributed to numerics (both different computational techniques and equilibrium processing) and some have their origin in different physical approximations. For example, the ideal MHD eigenfunction calculated by NOVA peaks at $\rho \approx 0.8$, while the ideal MHD eigenfunction calculated by the GATO code (Fig. 3 of Ref. 47) peaks at $\rho \approx 0.6$. Despite these differences, the ideal MHD eigenfunctions are qualitatively similar and both lack the large central wavefields predicted by the gyrokinetic code. The dramatic differences in Figs. 2–3 indicate that comparison with internal measurements can provide a sensitive test of the validity of the theoretical treatments.

III. SOFT X-RAY PROFILES

The soft x-ray emissivity S depends on the electron density n_e , the density of impurity ions n_I , and the electron temperature T_e . Since Alfvén modes are low frequency

waves, the electron and ion fluids are expected to oscillate with the field, so oscillations in the soft x-ray emissivity \bar{s} are related to the radial displacement of the field ξ by $\bar{s} = \xi \cdot \nabla s$.

At the time of the experiment, the poloidal soft x-ray array at DIII-D (Ref. 48) consisted of two sets of silicon diodes. The horizontal camera had 32 channels, while the vertical camera had 16 channels. All of the channels measured the slowly varying “dc” soft x-ray emission, but only half of the channels were instrumented to measure high-frequency fluctuations. The frequency response of the instrumented channels was 250 kHz.

The dc emissivity profile s is inferred from inversion of the chordal measurements. Because the data are too sparse for a complete tomographic inversion, s is assumed to be an axisymmetric function of the magnetic flux (Fig. 4). (Actually, in rotating plasmas, centrifugal effects cause an outward shift of the impurity density n_I ,⁴⁹ but we ignore this effect in these plasmas with subsonic carbon impurities.) The geometry of the flux surfaces is obtained from the EFIT equilibrium reconstruction. The plasma is first partitioned into a finite number of flux zones then the path length of each soft x-ray chord through each zone is computed. The results are assembled into a response matrix. A vector of the measured chord-averaged signals S_x is also constructed. The emissivity profile is then obtained by matrix inversion using singular value decomposition. To check the inversion, the expected chord-averaged signals S are compared with the measured values S_x (Fig. 5). The agreement between S and S_x is optimized for 9–11 flux zones (with subsequent smoothing of the s profile). The biggest discrepancy between the measured profiles and the simulated profiles is in the horizontal camera. For this symmetric plasma that was limited on the inner wall, the simulated profiles are vertically symmetric, but the actual emission from the upper half of the plasma is somewhat larger than the emission from the lower half.

To obtain the amplitude of the fluctuations \tilde{S}_x , the fast Fourier transform of the cross power is computed for an $n=5$ TAE mode with a frequency of 118 kHz in the laboratory frame. (The toroidal mode number n is inferred from measurements with a toroidal array of eight unequally spaced magnetic probes.) The data with the largest signal to noise ratio are from later in the discharge (2.17 s) than the time of the theoretical calculations (1.875 s) but the differ-

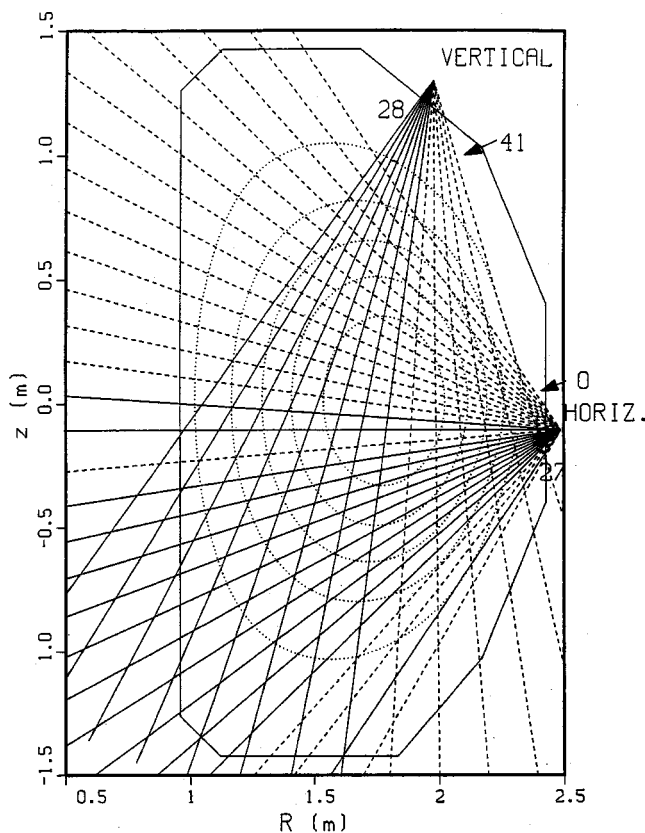


FIG. 4. Elevation of the DIII-D vessel showing the sightlines for the vertical and horizontal soft x-ray cameras. Channels with both DC and TAE signals are represented by solid lines, while channels with only dc signals are represented by dashed lines. Channel numbers employed in Fig. 5 are indicated. Also shown are some of the flux surfaces (dotted curves) in discharge 71524.

ences in plasma parameters are small ($<10\%$ changes in density, β , β_f , and central q). The uncertainty in the amplitude is estimated from the coherency and from the amplitude at 110 kHz (in a “valley” between the TAE peaks in spectrum); the two methods yield comparable error estimates. For both the horizontal and vertical cameras, the signals are an order of magnitude larger for the central channels than for the edge channels.

To compare with the theoretical predictions, the calculated perturbation ξ for the $n=5$ mode is converted to an image on a uniform grid (Fig. 3) and multiplied by the gra-

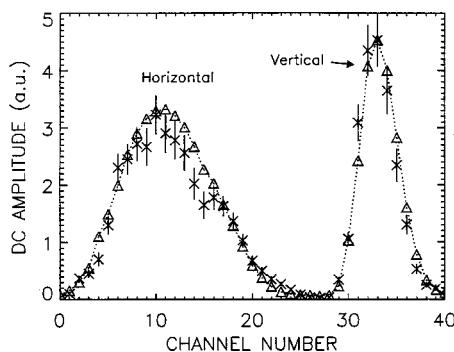


FIG. 5. Average amplitude of the measured (\times) and simulated (Δ) chord-averaged signals at the time of the TAE burst.

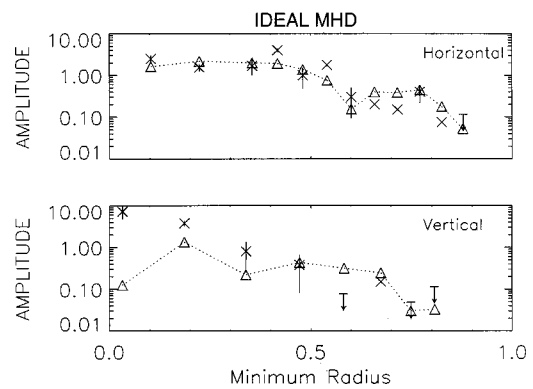


FIG. 6. Measured (\times) and simulated (Δ) chord-averaged signals for the 118 kHz, $n=5$, TAE mode plotted as functions of minimum radius. (The minimum radius is defined as the ρ of closest approach to the magnetic axis for a given channel.) The simulation is for the $n=5$ linear eigenfunction calculated by NOVA-K; the normalization of the simulated data minimizes χ^2 . The uncertainties in the simulated signals associated with uncertainties in the emissivity profile s are comparable to the size of the symbols. The downward arrows represent the upper bound for channels without detectable signal.

dient of the dc emissivity ∇s . The expected signals are obtained by integrating $\xi \cdot \nabla s$ over the detector sightlines. The resulting comparisons are shown in Figs. 6–8. The profile simulated using the NOVA eigenfunction has less variation between edge channels and central channels than the experimental data; also, the predicted signals for the horizontal camera are larger than the predicted signals for the vertical camera, in contradiction to the data. The NOVA eigenfunction peaks strongly near the inner and outer midplane, but the soft x-ray data are inconsistent with strong peaking at the periphery. [Use of the ideal MHD eigenfunction computed by GATO (Ref. 47) yields a similar conclusion.] The contrast between edge channels and central channels is greater for the eigenfunction calculated by the gyrofluid code, but is still less than the measured contrast. The contrast between edge and central channels predicted by the PENN code is comparable to the experimental observations. This reflects the relatively large central displacement of the PENN eigenfunction.

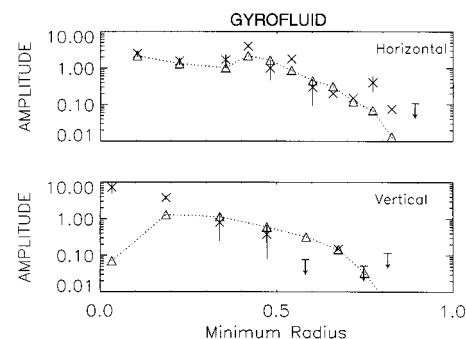


FIG. 7. Measured (\times) and simulated (Δ) chord-averaged signals for the 118 kHz, $n=5$, TAE mode. The simulation is for the $n=5$ linear eigenfunction calculated by the gyrofluid code; the normalization of the simulated data minimizes χ^2 . The uncertainties in the simulated signals associated with uncertainties in the emissivity profile s are comparable to the size of the symbols.

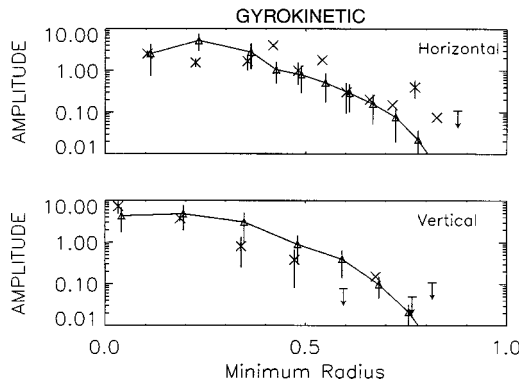


FIG. 8. Measured (\times) and simulated (Δ) chord-averaged signals for the 118 kHz, $n=5$, TAE mode. The simulation is for the $n=5$ linear eigenfunction calculated by the PENN code; the normalization of the simulated data minimizes χ^2 . The error bars on the simulated signals represent the sensitivity to uncertainties in the position of the $q=1$ surface and to the pressure gradient near $q=1$.

Qualitatively, the data agree best with the PENN prediction, but the quantitative agreement is poor for all of the calculated eigenfunctions. The experimental uncertainties are known accurately, but the uncertainties in the theoretical predictions are difficult to quantify. The sensitivity of the predictions to the inversion of the dc emissivity s was studied by using different EFIT equilibria and by varying the order of the inversion matrix. Because the predicted signals are dominated by the edge, the NOVA predictions were sensitive to these variations, but the PENN and gyrofluid predictions were scarcely affected. The sensitivity of the eigenfunction itself was studied three ways. For NOVA, pressure, density, and q profiles at the extremes of the experimental errors were generated and employed in a series of runs, but all of the calculated eigenfunctions peaked strongly at the edge. For the gyrofluid code, the sensitivity to uncertainties in the gap structure was artificially explored by varying the assumed value of v_{\parallel}/v_A ; this shifts the location of the peak of the eigenfunction. The differences in simulated signals for v_{\parallel}/v_A between 0.3 and 0.85 are comparable to the symbol sizes in Fig. 7. The PENN prediction is sensitive to the position of the $q=1$ surface and to the pressure gradient in this region, which have experimental uncertainties of approximately 10% and 20%, respectively. Estimates of the likely effect of these errors were used to distort the calculated eigenfunction (Fig. 3), and the effect on the simulated soft x-ray signals was explored. (The PENN prediction is too computationally expensive for a rigorous sensitivity study.) This sensitivity study suggests that, with judicious adjustment of the input parameters within experimental uncertainties, the PENN eigenfunction *could* be made consistent with the measured profile.

IV. PARTICLE TRANSPORT SIMULATIONS

A. Simulation details

The Hamiltonian guiding-center code ORBIT (Ref. 50) is used to simulate the effect of TAE modes on beam ion confinement. In ORBIT, an ensemble of particles are “born” according to a user-defined probability distribution then the

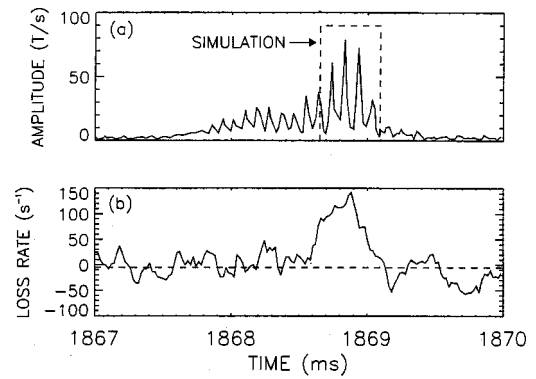


FIG. 9. (a) Envelope of a digitally-filtered (80 kHz high pass) \dot{B}_θ signal in discharge 71524. The probe is mounted near the midplane close to the outer wall. The transport simulations (dotted line) assume constant TAE amplitude, for the duration of the simulations, ~ 0.43 ms. (b) Derivative of the 2.5 MeV neutron signal $-(dS_n/dt)/(S_n)$. The signal is smoothed (0.3 ms averaging) prior to differentiating, so the actual duration of the losses may be shorter than shown. The dotted line indicates the average slope between TAE bursts (the recovery rate of the neutron signal).

code follows the trajectories of the particles' guiding centers. Particles whose guiding centers cross the plasma boundary before the end of the run are judged lost. The same EFIT equilibrium used with the other codes is adapted for these simulations, with both axisymmetry and up-down symmetry assumed.

Establishing the length for a run to simulate the burst is nontrivial. Data from a typical burst appear in Fig. 9. The TAE mode amplitude evolves rapidly, with the entire burst persisting for longer than a millisecond. However, as in the case shown in Fig. 9, the bulk of the losses generally occur in the 0.1–0.3 ms range when the mode is near its maximum amplitude. In the simulations, the mode amplitude is assumed constant in time and the total run duration is set at $\sim 430 \mu\text{s}$, or about 30 toroidal transits for a deeply passing 75 keV deuteron. (The nominal transit time is $\tau_{\text{trans}} \approx 4.3 \mu\text{s}$.) The equations of motion are solved at intervals of $\sim \tau_{\text{trans}}/300$, and the energy change per particle is limited to less than 20%. The run time is sufficiently short compared to any characteristic collision time that no collisional effects are included in the simulations. Beam fueling is also ignored.

For the beam ion distribution function, the pitch $\lambda = v_{\parallel}/v$, energy E , poloidal angle θ , and minor radius along the midplane r of individual particles are randomly generated using a Monte Carlo prescription that “fits” the population to a specified probability distribution. The code TRANSP (Ref. 51) is used to determine the initial distribution of beam ions for this discharge (with the additional assumption that the particles are uniformly distributed in θ). In the TRANSP calculation, profiles of the electron density and temperature were used to calculate the beam deposition. Because we are inferring beam ion confinement from the 2.5 MeV neutron measurement, only particles above the injection half-energy ($E > 38$ keV) are considered. The initial particle distribution used in this study is shown in Fig. 10 and is in essence a classical slowing down distribution. Most ions are on co-going passing orbits. The particle population is calculated in the lab frame, while the simulations are done the plasma

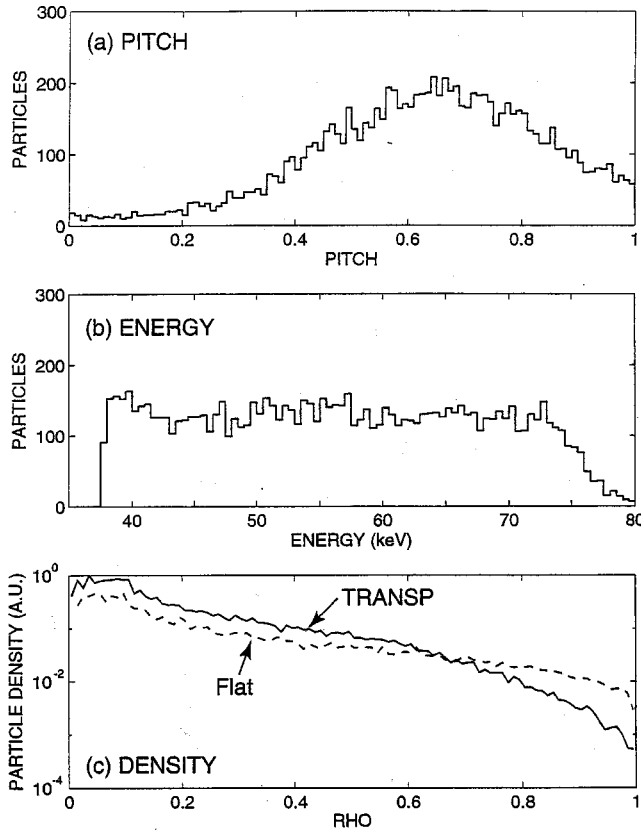


FIG. 10. Birth distribution of 10 000 deuterium beam ions generated from a probability distribution calculated by TRANSP using a Monte Carlo prescription. Shown are histograms for the population in terms of (a) pitch and (b) energy, as well as the (c) radial profile of the particle density from TRANSP (solid) and using a radially flat profile (dashed). Pitch is defined as v_{\parallel}/v . All particles are launched along the outer midplane, $\theta=0$.

frame, but the Doppler shift in particle velocity is neglected since the plasma rotation of ~ 10 kHz is small compared to typical transit frequencies. For all simulations, 10 000 birth particles are initially generated.

In general, an instability can cause spatial transport through both its magnetic field and its electric field. For the magnetic field, the TAE eigenfunction is introduced as an oscillating perturbation to the equilibrium field. In this formalism, the coordinate system is defined by three position variables (the poloidal flux ψ_p , the poloidal angle θ , and toroidal angle ζ) and a Jacobian of the form $J \sim 1/B_0^2$.⁵² (\mathbf{B}_0 represents the unperturbed equilibrium field.) The perturbation $\delta\mathbf{B}$ is introduced into the equations of motion using the scalar function α which is related to the perturbation through $\delta\mathbf{B} = \nabla \times \alpha \mathbf{B}_0$. The code expects coefficients $\alpha_{nm}(\psi_p)$ for a Fourier decomposed scalar perturbation $\alpha(\psi_p, \theta, \zeta) = \sum \alpha_{nm}(\psi_p) \sin(n\zeta - m\theta + \omega t)$, where ω is the frequency of the mode, and t is the time. In the ideal MHD case, NOVA's solution is given as the radial component of the displacement vector $\xi_r = \xi \cdot (\nabla \psi_p / |\nabla \psi_p|)$. To interface properly with ORBIT, ξ_r is converted into α using³¹

$$\alpha_{nm} = \frac{R_o(m-nq)}{JB^2} \xi_{nm}, \quad (1)$$

TABLE I. Summary of peak values of $\delta B_r/B_0$ obtained using different approaches.

Data source	$\delta B_r/B_0$
Mirnov data and ideal MHD eigenfunction	$< 2 \times 10^{-4}$
Soft x-ray data	$> 0.7 \times 10^{-4}$

which assumes that ξ_r has been Fourier-decomposed in θ and ζ with Fourier coefficients $\xi_{nm}(\psi_p)$.

In the ideal MHD model, electrons rapidly short out the parallel electric field, so the electric field is induced by the time-dependent magnetic perturbation. In the plasma frame, the equilibrium electric field is negligible. The perturbed potential ϕ_1 is Fourier analyzed and the coefficients are given by

$$\phi_{nm}(\psi_p, t) = \frac{-\alpha_{nm}\omega_{nm}}{n-m/q}. \quad (2)$$

The singularity when $q=m/n$ is a by-product of the ideal MHD model. To smooth the potential inside the magnetic island at the rational surface, the replacement

$$n-m/q \rightarrow \frac{(n-mq)^2 + \delta\psi_p^2}{n-mq}$$

is made, where $\delta\psi_p = 4\sqrt{q'}|\alpha_{nm}|/\epsilon$ is the nominal island width.

To evaluate the effect of the instability on the neutron rate, we write out the confined particle distribution at the end of each run and calculate the beam-plasma reaction probability $n_d \langle \sigma v \rangle_{b-p}$ of each particle using profiles of deuterium density n_d and temperature T_d inferred from experimental data. (From TRANSP, the neutron signal is dominated by beam-plasma reactions with $< 5\%$ contributions from beam-beam and thermonuclear reactions.) The beam-plasma reactivity is approximately⁵³ $\langle \sigma v \rangle_{b-p} \approx [1 + c_1 T_d/E] \sigma v$, where σv is evaluated at the injection energy E and c_1 is a constant that depends on E .

B. Determining the perturbation strength

The available experimental measurements of the mode amplitude are the magnetic perturbation δB_θ near the vacuum vessel and the amplitude of the soft x-ray measurements. In this subsection, these measurements are related to the Fourier components α_{mn} employed in the simulation. Our conclusions are summarized in Table I.

The maximum amplitude of δB_θ measured at a coil along the outer midplane is ~ 0.6 G; the toroidal field is ~ 0.8 T. The magnetics signal is affected by vessel currents so the equivalent vacuum field is about half as large. To estimate $|\delta B|$ for the NOVA eigenfunction, we use a formula derived from a multipole expansion about the magnetic axis, $|\delta B_{r,m}| \approx |\delta B_{\theta,wall}|(b/r)^{m+1}$, where b is the distance from the magnetic axis to the coil, and $r \approx sa$ is the distance from the magnetic axis to the radius of maximum amplitude for the m th poloidal harmonic. For the $n=3$ case, the largest contributions to the field at the coil are from the $m=6$ and $m=7$ poloidal harmonics. The inferred maximum value of

the total perturbation is $\delta B_r/B_0 \sim 2 \times 10^{-4}$. In the experiment, several toroidal harmonics are simultaneously excited. For the NOVA simulations, the maximum values of $\delta B_r/B_0$ inferred for the $n=3,4,5$ toroidal components are in the ratio 1.00:1.11:0.74. The measured mode frequencies in the plasma frame are nearly identical, so a value of 64 kHz is employed for all three toroidal harmonics.

An independent estimate of the internal perturbation amplitude is available from the soft x-ray data. The measured fluctuation in signal at the TAE frequency is \tilde{S}_x . The displacement ξ_r of the flux surface intersected by the soft x-ray chord is $\xi_r \approx \tilde{S}_x / \nabla S_x$, where ∇S_x is the gradient of the dc soft x-ray emissivity at the innermost portion of the soft x-ray chord. If the perturbed field is “tied” to the fluid, as expected for a shear Alfvén wave, the perturbed field is $\delta B_r = B_0 k_{\parallel} \xi_r$, where the parallel component of the wave vector $k_{\parallel} = 1/2qR$ for a TAE. Thus, $\delta B_r/B_0 \approx \xi_r/2qR$. The maximum measured value of ξ_r for the available chords is ~ 0.4 mm, which implies a maximum perturbation $\delta B_r/B_0 \approx 0.7 \times 10^{-4}$. Since the available chords may miss the maximum perturbation and the measurements are chord averaged, this value is an approximate lower bound.

To relate the amplitude of the mode used in the code to the measured value of δB_r , this amplitude needs to be converted into physical units by relating the scalar function α to the perturbation strength $\delta B_r/B_0$. The equilibrium magnetic field in the (ψ_p, θ, ζ) coordinate system can be expressed as⁵⁴ $B_0 = g(\psi_p) \nabla \zeta + I(\psi_p) \nabla \theta + \delta(\psi_p, \theta) \nabla \psi_p$. In this coordinate system, the Jacobian is given by $J = (I + gq)/B_0^2$. Assuming that the minor radius $r \approx \sqrt{2\psi_p/B_0}$, we can express the radial component of the perturbation δB_r in terms of the Fourier decomposed scalar perturbation, α_{nm} , as

$$\frac{\delta B_r}{B_0} \approx \sum \frac{\alpha_{nm}}{F_{nm}} \cos(n\zeta - m\theta + \tilde{\omega}t), \quad (3)$$

with $F_{nm} \equiv (r/R_0)[(I + gq)/(nI + mq)]$ and R_0 as the plasma major radius. Only the peak value is required to make the conversion from code to physical units. For the $n=3$ mode, we evaluate Eq. (2) for ζ , θ , and t set to 0 and find the ratio between the peak values of $\delta B_r/B_0$ and α is 7.4×10^{-4} .

C. Simulation results

The simulation results using all three ($n=3-5$) toroidal components from NOVA are given in Fig. 11. Near the measured peak mode amplitude ($\delta B_r/B_0 \approx 2 \times 10^{-4}$) and using the TRANSP distribution, particle losses are nonexistent and neutron losses are minuscule. Even at a significantly stronger amplitude ($\delta B_r/B_0 \approx 5 \times 10^{-3}$), neutron losses only reach $\sim 4\%$, still below the observed 6%–8% drop in the neutron emission. Additional runs are conducted at frequencies close to the observed TAE frequency, i.e., $f_{\text{TAE}} \pm 50$ kHz at ~ 10 kHz intervals, with the perturbation strength set at the experimental mode amplitude to check for the presence of a transport resonance, but no significant particle losses are seen.

A lower frequency fishbone is present during the burst along with the TAE (Fig. 1), which may result in a radial

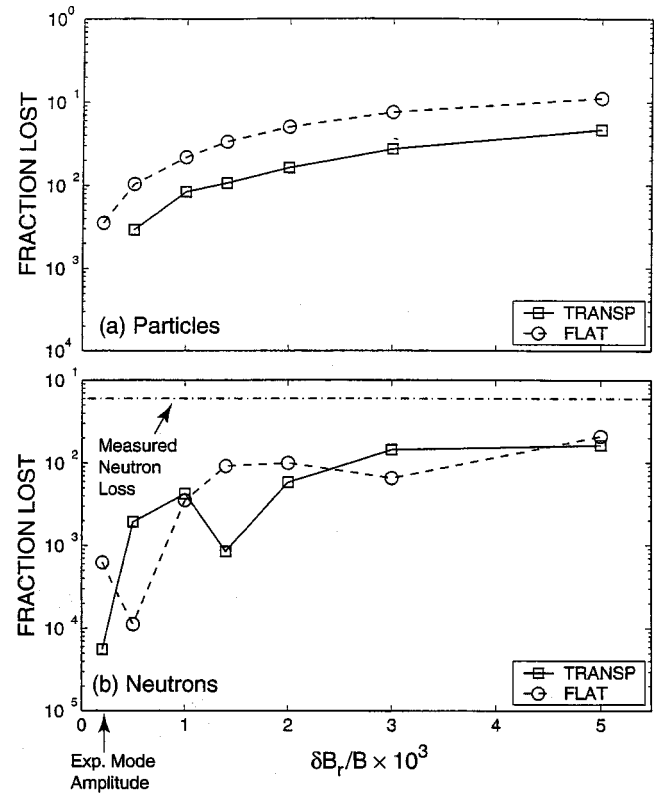


FIG. 11. Fraction of lost (a) particles and (b) total neutrons in the simulations using the $n=3-5$ eigenfunctions from NOVA with the TRANSP-calculated particle distribution (squares) and the same distribution but with a flat profile in minor radius (circles). The losses are plotted as functions of perturbation strength. The measured mode amplitude and drop in the 2.5 MeV neutron rate (dashed-dotted) are also indicated.

flattening of the beam ion distribution profile and lead to enhanced transport. To test this hypothesis, a distribution with an artificially flat profile in minor radius [$f_{\text{beam}}(r) \sim \sqrt{1-r}$] was used as the birth distribution. Simulations with the flattened radial distribution resulted in a larger particle loss as compared with the TRANSP case [Fig. 11(a)] but little change in the predicted drop in neutron emission [Fig. 11(b)]. Therefore, at least for this ideal MHD case, any prior redistribution of the energetic particle population by preceding TAE and fishbone bursts has little effect on the predicted neutron reduction. As before, additional runs about the TAE frequency were conducted with a similarly null result. For the record, particle losses with both distributions scaled linearly in δB_r over the range of mode amplitudes given in Fig. 11, with correlation coefficients for the least squares fit of 0.999 and 0.996 for the TRANSP and radially flattened cases, respectively.

V. DISCUSSION

A. Origin of the discrepancy

Neither the soft x-ray data nor the beam-ion loss measurements agree quantitatively with the predictions made using the ideal MHD, gyrofluid, and gyrokinetic models. This suggests that either the experimental data, the comparisons, or the theoretical models are erroneous.

The data are unlikely culprits. The soft x-ray measurements are valid. At other frequencies in the same discharge, normal $m=3$, $n=2$ tearing modes are observed; also, the profile for “BAEs” (Ref. 55) differs considerably from the TAE profile. There is also no question that beam ions are really lost under these conditions, as the neutron data are corroborated by stored energy, foil bolometer, and active charge exchange diagnostics,^{40,55} as well as by observations of internal damage to vacuum vessel components.⁴⁰ The observation that the mode amplitude is relatively small is well documented as well: when “chirping modes” (modes with frequencies that change by a factor of 2 in a millisecond) cause 8% drops in neutron emission, the magnetic perturbation δB_θ is an order of magnitude larger than during TAE activity.⁵⁶ In our analyzed discharge (71524), the soft x-ray fluctuation from the $n=2$ tearing mode was two orders of magnitude larger than the TAE signal.

Systematic errors in the comparisons are a more plausible culprit. There are two main caveats in the soft x-ray comparison. First, because of the coarseness of the array, the dc emissivity s was assumed to be a flux function. In reality, the emissivity, which depends linearly on the distribution of impurities, may exhibit significant poloidal asymmetries. In the comparison, the predicted signals are multiplied by the gradient of the dc emissivity, so the sensitivity to errors in s is appreciable. Second, the reported soft x-ray measurements are from later in the discharge (2.17 s) than the beam-ion loss data and theoretical calculations (1.875 s). (Because the beam-ion losses caused an influx of impurities, the signal to noise ratio of the soft x-ray data is superior later in the discharge.) The plasma parameters at these two times are similar, however, so this is probably not a major source of error.

There are three major caveats in the comparison with the beam-ion loss data. First, it was not feasible to retain all of the poloidal and toroidal harmonics that are excited in the experiment. The largest harmonics were employed in the reported simulations and tests indicate only weak sensitivity ($\leq 50\%$ enhancement of total losses) to the inclusion of additional modes of comparable amplitude, but this is a potential source of systematic error. The second caveat is associated with the choice of the beam-ion distribution function. Most of the simulations used the classical beam-ion distribution calculated by TRANSP. In the experiment, the losses occur in repetitive bursts, so prior bursts almost certainly altered the distribution function prior to the analyzed burst. Available measurements suggest anomalous pitch-angle scattering is relatively weak, so these modifications likely consist of a broadening of the profile (due to internal transport) and a reduction in low-energy beam ions (due to prior losses). Both effects are expected to increase the calculated losses, although artificial flattening of the profile resulted in only a small change (Fig. 11). The third caveat is that the bursts had concurrent fishbone activity. Experimentally in DIII-D,⁴⁰ for a given amplitude TAE mode, the measured losses are generally higher during combined fishbone and TAE activity than during TAE activity alone, the losses depend much more strongly on the TAE amplitude than on the fishbone amplitude, and losses are negligible ($<1\%$) for pure fishbone

modes. The simulation with the flat beam-ion profile was intended to mimic the effect of fishbone activity, but conceivably there is a synergistic effect that was not included in our simulations.

The third possibility is that the experimental eigenfunction really differs from the theoretical eigenfunctions. This hypothesis is compatible with prior studies. Although rough consistency between theoretical eigenfunctions and measurements have been reported,^{20–22,57} the most detailed comparisons found discrepancies.^{21,23} An earlier study of discharge 71524 concluded that the predictions of the MHD model disagree in both amplitude and phase with the poloidal distribution of edge magnetic fluctuations, while the gyrokinetic model gives satisfactory agreement for the amplitude but not the phase.²³ Thus, three sets of data—soft x-ray, beam-ion loss, and poloidal magnetic—are all inconsistent with the theoretical predictions for this discharge.

Why might the eigenfunctions be incorrect? It is known from stability studies of discharge 71524 that radiative damping (or related effects) is needed to account for the observed power threshold.^{58,59} Also, to obtain agreement with JET measurements of mode damping it was necessary to include mode coupling to kinetic Alfvén waves.^{60–62} This effect is not included in the ideal MHD or gyrofluid models and may need further refinements in the PENN treatment. Another possibility is that energetic-particle effects associated with the beam ions modify the eigenfunction. (The beam beta is comparable to the thermal beta in this discharge.) A final possibility is that the use of linear eigenfunctions does not properly model the experiment. Experimentally, the different toroidal modes tend to lock and rotate together, even though their expected linear frequencies differ.³⁶

B. Mechanism of beam-ion loss

A TAE mode can transport beam ions out of a tokamak plasma in several ways:

- A class of passing particles can circulate with the mode and resonantly drift out of the plasma via an $\mathbf{E} \times \mathbf{B}$ drift, similar to mode-particle pumping for fishbones.⁶³ The losses would scale as $\delta B_r/B_0$ and require only a few transits for losses to occur.
- Countergoing ions can be resonantly converted into large banana orbits that intersect the wall as the particle interacts with the wave over a short period of time.^{30,31} The losses scale as $(\delta B_r/B_0)^2$. For significant ($>1\%$) losses, however, the time of the run needs to be long compared to the transit time (the time it takes for a passing particle to complete one circuit around the torus) as particles need to slow down or pitch-angle scatter into this resonant region of phase space.
- The particles are born near a loss boundary in phase space and their resonant interaction with the wave causes them to cross that boundary into a loss orbit;³⁰ alternatively, some particles may be sent into a ripple-trapped orbit before being lost.⁶⁴ The overall losses can occur within a few transits of the particle's birth and are significant only for a short period of time.
- Finally, multiple harmonics can lead to islands in the

particle's phase space which, at sufficiently large perturbations, can overlap and the particle's motion can become stochastic.⁶⁵ This mechanism is a threshold effect and occurs once the mode strength creates large enough islands.

Considering the short time in which the losses occur, we can eliminate mechanism (b) as a possible explanation of the dominant loss mechanism during this burst. In the simulations, all the other mechanisms are explored, except for particles getting nudged into a ripple-trapped orbit [as in mechanism (c)] since ripple is not included in the calculation. (DIII-D has 24 coils so the ripple-trapping region is relatively small.) The calculated losses for the MHD eigenfunction scale approximately linearly with δB_r and the pitch of lost particles tends to be >0.7 , suggesting that resonant convective losses [mechanism (a)] predominate in these simulations. Since the calculated increase in losses with increasing δB_r is modest, we can conclude that the simulations never reached a stochastic threshold, as would be the case for mechanism (d).

Based on linear scaling of the losses with δB_r and on the ~ 10 cm radial step size of the final loss orbit, it was previously concluded⁴⁰ that mechanism (a) predominates in the experiment. Because the calculated losses are inconsistent with the measurements, the present simulations do not definitively establish the mechanism of beam-ion transport.

VI. CONCLUSIONS

All three codes compute a mode frequency close to the experimentally measured frequency but, due to the different physics assumptions, the predicted eigenfunctions are radically different (Figs. 2–3). Eigenfunction measurements provide a more stringent test of theoretical models than frequency measurements alone.

Predictions based on the linear MHD eigenfunction are inconsistent with soft x-ray, poloidal magnetic, and beam-ion loss data for this discharge. Apparently, the actual eigenfunction is not as large near the periphery as predicted. The gyrokinetic eigenfunction is in better qualitative agreement with the soft x-ray measurements than the ideal MHD model, but the quantitative agreement is only fair. It is possible that systematic uncertainties account for the discrepancy.

Particle simulations based on the MHD eigenfunction predict several times smaller losses than observed experimentally. Possible explanations include the synergistic effect of fishbone activity and nonlinear couplings between different toroidal modes. The most likely explanation is that the inductive electric field predicted by MHD fails to model the actual electric field. The amplitude of the magnetic perturbation ($\delta B/B \sim 10^{-4}$) is very small; typically, a value of $\delta B/B \sim 10^{-3}$ is required for appreciable transport in simulations. In the experiment, the likely transport mechanism is the resonant $\mathbf{E} \times \mathbf{B}$ drift. Kinetic modifications of the eigenfunction may produce appreciable electric fields, facilitating radial transport. Future work should concentrate on simulations employing the full magnetic and electric fields predicted by codes that retain kinetic effects.

ACKNOWLEDGMENTS

Guido Huysmans generously shared his Interactive Display Language (IDL) programs for analysis of JET soft x-ray data, which served as a model for the analysis in Sec. III. The support of the DIII-D team and insightful suggestions by Liu Chen and Ted Strait are also gratefully acknowledged.

This work was supported by General Atomics subcontract No. SC-G903402 to United States Department of Energy Contract No. DE-AC03-99ER54463.

- ¹ITER Physics Expert Group on Energetic Particles, Heating, and Current Drive, ITER Physics Basis Editors, Nucl. Fusion **39**, 2471 (1999).
- ²J. P. Goedbloed, Phys. Fluids **18**, 1258 (1975).
- ³C. Z. Cheng, L. Chen, and M. S. Chance, Ann. Phys. (N.Y.) **161**, 21 (1985).
- ⁴G. Y. Fu and J. W. van Dam, Phys. Fluids B **1**, 1949 (1989).
- ⁵K. L. Wong, R. J. Fonck, S. F. Paul, D. R. Roberts, E. D. Fredrickson, R. Nazikian, H. K. Park, M. Bell, N. L. Bretz, R. Budny, S. Cohen, G. W. Hammett, F. C. Jobes, D. M. Meade, S. S. Medley, D. Mueller, Y. Nagayama, D. K. Owens, and E. J. Synakowski, Phys. Rev. Lett. **66**, 1874 (1991).
- ⁶W. W. Heidbrink, E. J. Strait, E. Doyle, G. Sager, and R. T. Snider, Nucl. Fusion **31**, 1635 (1991).
- ⁷M. N. Rosenbluth, H. L. Berk, J. W. van Dam, and D. M. Lindbreg, Phys. Rev. Lett. **68**, 596 (1992).
- ⁸F. Zonca and L. Chen, Phys. Rev. Lett. **68**, 592 (1992).
- ⁹R. R. Mett and S. M. Mahajan, Phys. Fluids B **4**, 2885 (1992).
- ¹⁰J. Candy and M. N. Rosenbluth, Nucl. Fusion **35**, 1069 (1995).
- ¹¹G. Vlad, F. Zonca, and F. Romanelli, Nucl. Fusion **35**, 1651 (1995).
- ¹²A. Jaun, J. Vaclavik, and L. Villard, Phys. Plasmas **4**, 1110 (1997).
- ¹³S. Briguglio, C. Kar, F. Romanelli, G. Vlad, and F. Zonca, Plasma Phys. Controlled Fusion **37**, A279 (1995).
- ¹⁴C. Z. Cheng, N. N. Gorenlenkov, and C. T. Hsu, Nucl. Fusion **35**, 1639 (1995).
- ¹⁵R. A. Santoro and L. Chen, Phys. Plasmas **3**, 2349 (1996).
- ¹⁶F. Zonca and L. Chen, Phys. Plasmas **3**, 323 (1996).
- ¹⁷N. N. Gorenlenkov, S. Bernabei, C. Z. Cheng, K. W. Hill, R. Nazikian, S. Kaye, Y. Kusama, G. J. Kramer, K. Shinohara, T. Ozeki, and M. V. Gorelenkova, Nucl. Fusion **40**, 1311 (2000).
- ¹⁸D. A. Spong, B. A. Carreras, and C. L. Hedrick, Phys. Plasmas **1**, 1503 (1994).
- ¹⁹K.-L. Wong, Plasma Phys. Controlled Fusion **41**, R1 (1999).
- ²⁰R. D. Durst, R. J. Fonck, K. L. Wong, C. Z. Cheng, E. D. Frederickson, and S. F. Paul, Phys. Fluids B **4**, 3707 (1992).
- ²¹R. Nazikian, G. Y. Fu, and Z. Chang, Phys. Plasmas **5**, 1703 (1998).
- ²²G. J. Kramer, M. Iwase, Y. Kusama, A. Morioka, M. Nemoto, T. Nishitani, K. Shinohara, S. Takeji, K. Tobita, T. Ozeki, C. Z. Cheng, G.-Y. Fu, and R. Nazikian, Nucl. Fusion **40**, 1383 (2000).
- ²³W. W. Heidbrink, A. Jaun, and H. A. Holties, Nucl. Fusion **37**, 1411 (1997).
- ²⁴A. Weller, in *Proceedings of the Seventh International Toki Conference on Plasma Physics and Controlled Nuclear Fusion*, edited by A. Miyahara, Y. Hamada, and K. Ida (North-Holland, New York, 1997).
- ²⁵W. W. Heidbrink, R. Hay, and J. D. Strachan, Phys. Rev. Lett. **53**, 1905 (1984).
- ²⁶F. Wising, D. Anderson, and M. Lisak, Plasma Phys. Controlled Fusion **34**, 853 (1992).
- ²⁷Y. Zhao and R. B. White, Phys. Plasmas **4**, 1103 (1997).
- ²⁸S. J. Zweben, D. S. Darrow, E. D. Fredrickson, G. Taylor, S. von Goeler, and R. B. White, Nucl. Fusion **39**, 1097 (1999).
- ²⁹B. C. Stratton, R. V. Budny, D. S. Darrow, R. K. Fisher, E. D. Fredrickson, G. Y. Fu, S. S. Medley, R. Nazikian, M. P. Petrov, M. H. Redi, E. Ruskov, G. Taylor, R. B. White, S. J. Zweben, and TFTR Group, Nucl. Fusion **39**, 1309 (1999).
- ³⁰D. J. Sigmar, C. T. Hsu, R. B. White, and C. Z. Cheng, Phys. Fluids B **4**, 1506 (1992).
- ³¹Y. Wu and R. B. White, Phys. Plasmas **1**, 2733 (1994).
- ³²L. C. Appel, H. L. Berk, D. Borba, B. N. Breizman, T. C. Hender, G. T. A. Huysmans, W. Kerner, M. S. Pekker, S. D. Pinches, and S. E. Sharapov, Nucl. Fusion **35**, 1697 (1995).

- ³³D. S. Darrow, S. J. Zweben, Z. Chang *et al.*, Nucl. Fusion **37**, 939 (1997).
- ³⁴A. Gibson and the JET Team, Phys. Plasmas **5**, 1839 (1998).
- ³⁵E. J. Strait, W. W. Heidbrink, A. D. Turnbull, M. S. Chu, and H. H. Duong, Nucl. Fusion **33**, 1849 (1993).
- ³⁶E. J. Strait, W. W. Heidbrink, and A. D. Turnbull, Plasma Phys. Controlled Fusion **36**, 1211 (1994).
- ³⁷W. W. Heidbrink, E. J. Strait, M. S. Chu, and A. D. Turnbull, Phys. Rev. Lett. **71**, 855 (1993).
- ³⁸W. W. Heidbrink, H. H. Duong, J. Manson *et al.*, Phys. Fluids B **5**, 2176 (1993).
- ³⁹M. S. Chu, J. M. Greene, L. L. Lao, A. D. Turnbull, and M. S. Chance, Phys. Fluids B **4**, 3713 (1992).
- ⁴⁰H. H. Duong, W. W. Heidbrink, E. J. Strait, T. W. Petrie, R. Lee, R. A. Moyer, and J. G. Watkins, Nucl. Fusion **33**, 749 (1993).
- ⁴¹L. L. Lao, H. St. John, R. D. Stambaugh, A. G. Kellman, and W. P. Pfeiffer, Nucl. Fusion **25**, 1611 (1985).
- ⁴²C. Z. Cheng and M. S. Chance, Phys. Fluids **29**, 3695 (1986).
- ⁴³G. Y. Fu, Phys. Plasmas **2**, 1029 (1995).
- ⁴⁴L. Charlton, J. A. Holmes, H. R. Hicks, V. E. Lynch, and B. A. Carreras, J. Comput. Phys. **63**, 107 (1986).
- ⁴⁵D. A. Spong, B. A. Carreras, and C. L. Hedrick, Phys. Plasmas **1**, 1503 (1994).
- ⁴⁶A. Jaun, K. Appert, J. Vaclavik, and L. Villard, Comput. Phys. Commun. **92**, 153 (1995).
- ⁴⁷A. D. Turnbull, E. J. Strait, W. W. Heidbrink, M. S. Chu, H. H. Duong, J. M. Greene, L. L. Lao, T. S. Taylor, and S. J. Thompson, Phys. Fluids B **5**, 2546 (1993).
- ⁴⁸R. T. Snider, R. Evanko, and J. Haskovec, Rev. Sci. Instrum. **59**, 1807 (1988).
- ⁴⁹K. L. Wong and C. Z. Cheng, Phys. Fluids B **1**, 545 (1989).
- ⁵⁰R. B. White and M. S. Chance, Phys. Fluids **27**, 2455 (1984).
- ⁵¹R. V. Budny *et al.*, Nucl. Fusion **34**, 1247 (1994).
- ⁵²R. B. White, Phys. Fluids B **2**, 845 (1990).
- ⁵³W. W. Heidbrink, P. L. Taylor, and J. A. Philips, Rev. Sci. Instrum. **68**, 536 (1997).
- ⁵⁴R. B. White, *Theory of Tokamak Plasmas* (North-Holland, New York, 1989).
- ⁵⁵W. W. Heidbrink, E. Ruskov, E. M. Carolipio, J. Fang, M. A. van Zeeland, and R. A. James, Phys. Plasmas **6**, 1147 (1999).
- ⁵⁶W. W. Heidbrink, Plasma Phys. Controlled Fusion **37**, 937 (1995); **37**, 1349 (1995).
- ⁵⁷W. W. Heidbrink, A. Fasoli, D. Borba, and A. Jaun, Phys. Plasmas **4**, 3663 (1997).
- ⁵⁸R. R. Mett, E. J. Strait, and S. M. Mahajan, Phys. Plasmas **1**, 3277 (1994).
- ⁵⁹A. Jaun, J. Vaclavik, and L. Villard, Phys. Plasmas **4**, 1110 (1997).
- ⁶⁰A. Jaun, A. Fasoli, and W. W. Heidbrink, Phys. Plasmas **5**, 2952 (1998).
- ⁶¹A. Jaun, A. Fasoli, J. Vaclavik, and L. Villard, Nucl. Fusion **39**, 2095 (1999).
- ⁶²A. Fasoli, D. Borba, B. Breizman, C. Gormezano, R. F. Heeter, A. Jaun, M. Mantsinen, S. Sharapov, and D. Testa, Phys. Plasmas **7**, 1816 (2000).
- ⁶³R. B. White, R. J. Goldston, K. McGuire, A. H. Boozer, D. A. Monticello, and W. Park, Phys. Fluids **26**, 2958 (1983).
- ⁶⁴R. B. White, Nucl. Fusion **35**, 1707 (1995).
- ⁶⁵H. E. Mynick, Phys. Fluids B **5**, 1471 (1993).